Variable Speed Operation of Brushless Doubly Fed Reluctance Machine Drive Using Model Predictive Current Control Technique

Karuna Kiran, *Student Member, IEEE*, and Sukanta Das, *Senior Member, IEEE*

***Abstract*—To accomplish an accurate and fast drive control, model predictive control (MPC) is considered as an effective control strategy nowadays. In MPC, the voltage vectors required for inverter control are evaluated considering the control objectives defined in terms of current or power or torque and flux. The optimal one is selected using an iterative prediction loop and applied in the next control interval. This form of MPC is simple in implementation and shows appreciable dynamic performance but the steady-state performance is compromised due to the limited availability of the number of voltage vectors, especially in the case of a two-level voltage source inverter. The present article explores the viability of the MPC approach for a new candidate such as a brushless doubly fed reluctance machine drive considering its secondary current as the control variable. Moreover, to tackle the steady-state inferiority issue, the duty-cycle control concept is inducted. In comparison to field-oriented control (FOC), the proposed scheme offers a straightforward solution for current control by replacing the inner current proportional–integral controllers and pulsewidth modulator with an optimization-based model predictive current controller. An extensive simulation study in MATLAB, vis-à-vis comparison with FOC scheme, and experimental validations justify the claims of the proposed work.**

***Index Terms*—Ac machines, brushless machines, current control, predictive control.**

Nomenclature

R_p, R_s	Primary and secondary winding resistances (Ω).
L_p, L_s, L_{ps}	Primary, secondary winding self and mutual inductances (H).
$\boldsymbol{v}, \boldsymbol{i}, \boldsymbol{\lambda}$	Voltage (V), current (A), and flux linkage (Wb-t) vectors.
ω_p, ω_s	Primary and secondary voltage/current angular frequency (rad/s).
ω_r,ω_{rm} N_r	Electrical, mechanical angular speed of rotor in (rad/s), and the number of revolution per minute (r/min).
θ_r	Angular position (rad) of rotor.
p_p, p_s, p_r	Primary, secondary, and rotor poles.
θ_p, θ_s	Primary and secondary reference frame position (rad).
P_p, Q_p	Primary active (W) and reactive (VAr) power.
k	Discrete time index.
Superscript	
r, s	Rotating and stationary frame quantities.
ref	Reference value of a variable.
Subscript	
p, s	Primary and secondary variables.
d, q	Direct and quadrature components of a variable.
a, b, c	Phase quantities.

Manuscript received June 20, 2019; revised September 21, 2019 and November 17, 2019; accepted December 26, 2019. Date of publication January 5, 2020; date of current version April 22, 2020. This work was supported by Science and Engineering Research Board (Department of Science and Technology), GOI, under Young Scientist Scheme YSS/2015/001670. Recommended for publication by Associate Editor H. Hofmann. *(Corresponding author: Sukanta Das.)*

The authors are with the Department of Electrical Engineering, Indian Institute of Technology (Indian School of Mines), Dhanbad 826004, India (e-mail: karunakiran108@gmail.com; asksukanta@iitism.ac.in).

Color versions of one or more of the figures in this article are available online at http://ieeexplore.ieee.org.

Digital Object Identifier 10.1109/TPEL.2020.2964007

I. Introduction

RECENT research works reveal that the brushless doubly fed machines (BDFMs) have the potential to efficiently substitute conventional slip ring induction machine (SRIM) and singly fed machines in variable-frequency speed control of motor drives and variable-speed constant-frequency generation systems [1]. The possibility of using low-cost fractionally rated inverter for limited speed range applications, improved reliability of brushless rotor [2], additional manifold modes of operation, flexible control of active and reactive power, crowbarless low-voltage ride-through grid integration capability, etc., are some distinct advantages to contest with the conventional choices [3].

The family of BDFMs has two sets of electrically independent three-phase stator windings sharing the common magnetic circuit with the involvement of a rotor. The primary winding is connected directly to a constant three-phase ac supply at power frequency. However, the secondary winding frequency is regulated through a bidirectional converter to achieve the desired speed [1]. In addition, both the windings have different pole configurations [4], [5]. Various types of BDFM topologies with different rotor structures are extensively studied in recent decades, such as cage rotor, reluctance rotor, wound rotor, and hybrid rotor. The characteristics of these rotor structures and some exemplary references are enlisted in [5]. The reluctance and cage rotors are two major types of rotor structures used in BDFMs. The BDFM drive having a reluctance rotor is simple in modeling and control and more robust and reliable in off-shore

applications where the accessibility of rotor is prohibited. In addition, a brushless doubly fed reluctance machine (BDFRM) is more efficient and exhibits a low saturation effect than a brushless doubly fed induction machine (BDFIM) due to the absence of rotor circuit and current. The comparative performance evaluation reveals that BDFIM has better starting and asynchronous characteristics; however, BDFRM exhibits better synchronous operation and doubly fed adjustable speed performance [6].

Scalar control (SC) [7], vector control (VC) [8], direct torque control (DTC) [9], and direct power control [10] strategies are well-established control methods in the literature of BDFRM. In the SC strategy, both the amplitude and frequency of the controlling parameters are adjusted proportionally maintaining flux constant. The scheme is a simple solution for narrow speed range applications where high performance is not of critical importance [7]. On the contrary, fast, accurate, and efficient control of the BDFRM drive can be achieved by the VC/field-oriented control (FOC) approach. The scheme is constrained to be executed in a rotating reference frame. In this scheme, the reference frame is oriented either along the direction of primary voltage vector [8] or flux vector [8], [9], [11], [12], [13] and the switching pulses for the converter are generated by the pulsewidth modulator (PWM) and at least three proportional—integral (PI) regulators. As a result, the primary and secondary sinusoidal variables are transformed into dc quantities in their natural reference frames. The primary field-oriented control (PFOC) strategy provides the inherent decoupling of torque and flux in motor drive applications and that of active and reactive power in generating system applications. The control rates and bandwidth of operation are restricted by the cascaded structure of speed and current controllers. Moreover, fine-tuning of PI controllers is required for the stable operation of the drive system over the entire control range.

In contrary to VC/FOC, the DTC approach is able to control the torque and flux directly with fast and accurate dynamics using modest structure. The voltage vector is directly selected from a predefined switching table on the basis of secondary flux, its position and torque. The implementation of DTC does not demand rotating axis transformations, current PI controllers, and PWM stage. Because of the direct pulse generation strategy, the scheme is suitable for the applications requiring high dynamic response. The variable switching frequency and high current and torque ripples attributed by the hysteresis controllers are the main drawbacks of DTC that can be curtailed by incorporating duty-cycle control [14].

The emergence of advanced control hardware platforms has made model predictive control (MPC) scheme as a promising alternative for the control of converters [15], [16] and electrical drives [17]. Hence, the different control aspects of this technique are the subject undergoing intense study for various machine drive control in recent decades. Principally in MPC, the discrete model of the system is incorporated for predicting the future behavior of the controlled variables, such as current [15], power [18] and torque/flux [17]. The scheme has the ability to deal with various constraints, such as overcurrent protection and switching frequency minimization in a natural way, if utilized suitably [17]. Moreover, it supports the operation of power electronic converter having discrete nature with the finite number of switching states and a digital signal processor (DSP), which controls in a sample-based routine. Based on the utilization of control variable in MPC algorithm, the scheme is classified broadly as model predictive current control (MPCC) [19]–[21], model predictive power control (MPPC) [18], and model predictive torque control (MPTC) [22]. The realization of MPCC and MPPC algorithms is more straightforward than MPTC because they assess only one type of variable (current or power error) decomposed in its real and imaginary components in the objective function. However, in MPTC, the linear combination of torque and flux errors need to be minimized simultaneously with equal importance that requires weighting factor tuning to compensate the differences in physical nature, units, and magnitudes of the variables [22]. With the ease of simplicity in theoretical structure and high-performance control, MPCC is drawing attention of researchers from different fields of electric drives including induction motors [21], [23], [27] brushless dc motors [24], and permanent magnet synchronous motors [19]–[20], [25], [26].

Conventional MPCC strategy, as proposed in [28], employs only one optimal voltage vector among all the feasible voltage vectors of an inverter during the entire control period. This may not guarantee the current error to be nullified and may cause pronounced current ripples in the case of two-level voltage-source-inverter (2L-VSI) fed drives in particular. Similar to DTC [14], the steady-state performance of the conventional single-vector-based MPCC can be improved by introducing the concept of duty-cycle control [25], [27]. Taking this fact into consideration, the concept of duty-cycle control is incorporated in the present work by applying one zero voltage vector along with an optimal active voltage vector obtained by the conventional MPCC algorithm during one control interval. Moreover, the hardware time delay is also compensated using a two-step prediction in order to improve the control accuracy. The proposed MPCC technique is validated with computer simulations in MATLAB/Simulink and experimentally using dSPACE-1103 controller board. A comparative theoretical analysis has been performed with respect to the FOC scheme to reveal the potential of the scheme in the steady-state and transient-state conditions. The robustness of the drive against parameter variations is also evaluated. The research work is expected to be a valuable contribution to the area of control of BDFRM drive.

The article is organized sequentially as follows. Section II elaborates the mathematical configuration of the proposed MPCC for BDFRM meticulously. In Section III , few relevant simulation and experimental results are shown to validate the effectiveness of the control scheme. Section IV deals with the comparative performance analyses of the drive under MPCC with FOC strategy under the same test conditions. In addition, the impact of the machine parameter variations has also been considered in the case of MPCC in this section. Finally, Section V concludes the findings of the present article.

II. Theoretical Development of the Proposed MPCC for Speed Control of BDFRM Drive

In this article, the stationary frame machine model is preferred in designing the controller to reduce the computational

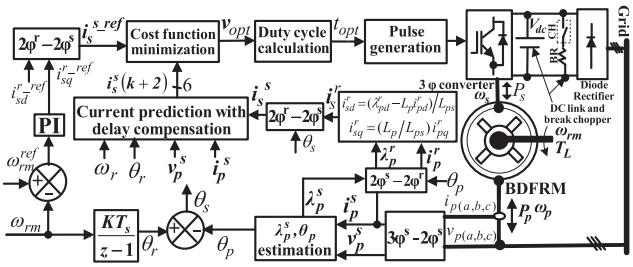

Fig. 1. Control diagram of the proposed MPCC scheme of BDFRM drive.

complexity and avoid the complications of coordinate transformations of inverter voltage vectors. The fundamental properties of the machine, as discussed in [8] and [13], are used for PFOC strategy based BDFRM drive control in this article.

The dynamic equations of the primary and secondary voltages of BDFRM represented in [4] are

$$v_{pd}^s = R_p i_{pd}^s + d\lambda_{pd}^s/dt - \omega_p \lambda_{pq}^s \tag{1}$$

$$v_{pq}^s = R_p i_{pq}^s + d\,\lambda_{pq}^s/dt + \omega_p \lambda_{pd}^s \tag{2}$$

$$v_{sd}^s = R_s i_{sd}^s + d\,\lambda_{sd}^s/dt - \omega_s \lambda_{sq}^s \tag{3}$$

$$v_{sq}^s = R_s i_{sq}^s + d\,\lambda_{sq}^s/dt + \omega_s \lambda_{sd}^s \tag{4}$$

where

$$\lambda_{pd}^s = L_p i_{pd}^s + L_{ps}\cos\theta_r i_{sd}^s + L_{ps}\sin\theta_r i_{sq}^s \tag{5}$$

$$\lambda_{pq}^s = L_p i_{pq}^s + L_{ps}\sin\theta_r i_{sd}^s - L_{ps}\cos\theta_r i_{sq}^s \tag{6}$$

$$\lambda_{sd}^s = L_s i_{sd}^s + L_{ps}\cos\theta_r i_{pd}^s + L_{ps}\sin\theta_r i_{pq}^s \tag{7}$$

$$\lambda_{sq}^s = L_s i_{sq}^s + L_{ps}\sin\theta_r i_{pd}^s - L_{ps}\cos\theta_r i_{pq}^s. \tag{8}$$

Fig. 1 presents the speed control scheme of the BDFRM drive using the proposed MPCC strategy. The scheme mainly consists of secondary reference frame position and secondary current estimation, secondary reference current generation and current control using the MPCC controller.

A. Secondary Reference Frame Position and Secondary Current Estimation

The secondary current components and their references are required to be transformed into their stationary counterparts as the rest part of the control algorithm is designed in the stationary reference frame. Consequently, the determination of the secondary frame position (θ_s) is mandatory. Under PFOC condition, the position of primary winding flux with respect to the stationary reference frame is considered as the primary reference frame position (θ_p), which is used for the calculation of θ_s [8]

$$\boldsymbol{\lambda_p^s} = \int (\boldsymbol{v_p^s} - R_s \boldsymbol{i_p^s})\, dt \tag{9}$$

$$\theta_p = \tan^{-1}(\lambda_{pq}^s/\lambda_{pd}^s) \tag{10}$$

$$\theta_s = \theta_r - \theta_p. \tag{11}$$

To reduce the number of current sensors and improve the quality of secondary current waveforms, the secondary current is estimated using primary variables

$$i_{sd}^r = (\lambda_{pd}^r - L_p i_{pd}^r)/L_{ps} \tag{12}$$

$$i_{sq}^r = (L_p/L_{ps})\, i_{pq}^r. \tag{13}$$

B. Secondary Reference Current Generation

Rotor speed feedback is compared with the reference speed and the error is fed to a PI controller to generate the q-axis secondary current reference ($i_{sq}^{r\_\mathrm{ref}}$) in ω_s rotating reference frame. The d-axis current reference ($i_{sd}^{r\_\mathrm{ref}}$) is set constant for the decoupled speed/torque and flux control. Moreover, it is set as zero to achieve maximum torque per inverter ampere (MTPIA) [8].

C. Current Control Using MPCC Controller

The proposed current controller system is designed mainly for the predictions of secondary current corresponding to the inverter active voltage vectors considering delay time compensation, selection of optimal active voltage vector through objective function minimization, calculation of optimal duty cycle for active voltage vector, and selection of switching states for 2L-VSI.

1) Current Prediction Considering Delay Time Compensation: In the digital implementation of MPCC, the controller output at kth instant cannot be applied instantly at $(k+1)$th instant due to the updating mechanism of DSPs and microcontrollers. Therefore, a one-step delay is compensated using a two-step prediction [29] to achieve better accuracy. The first-step prediction is considered for the delay compensation.

As the secondary current is used as a control variable in the proposed algorithm; therefore, the derivatives of the secondary current components can be developed by substituting (5)–(8) into (1)–(4) and rearranging as

$$d\,i_{sd}^s/dt = (1/a) \times \left\{v_{sd}^s - bv_{pd}^s - cv_{pq}^s + di_{pd}^s - ei_{pq}^s - R_s i_{sd}^s + fi_{sq}^s\right\} \tag{14}$$

$$di_{sq}^s/dt = (1/a) \times \left\{v_{sq}^s - cv_{pd}^s + bv_{pq}^s - ei_{pd}^s - di_{pq}^s - fi_{sd}^s - R_s i_{sq}^s\right\} \tag{15}$$

where

$$\left.\begin{aligned} a &= \sigma L_s \\ b &= (L_{ps}\cos\theta_r)/L_p \\ c &= (L_{ps}\sin\theta_r)/L_p \\ d &= (\omega_r L_p L_{ps}\sin\theta_r + R_p L_{ps}\cos\theta_r)/L_p \\ e &= (\omega_r L_p L_{ps}\cos\theta_r - R_p L_{ps}\sin\theta_r)/L_p \\ f &= L_s(\omega_r - \sigma\omega_p), \quad \sigma = 1 - L_{ps}^2/(L_p L_s) \end{aligned}\right\}. \tag{16}$$

In this article, Heun's method [30] is used to discretize (14), (15) for higher accuracy than Euler's first-order discretization [28]. The method involves two stages called prediction and correction, respectively. The predicted secondary currents as

obtained by the Euler's first-order discretization are considered as the outcomes of the prediction stage. Let they be represented as $i_{sd}^{s*}(k+1)$ and $i_{sq}^{s*}(k+1)$, respectively, where

$$i_{sd}^{s*}(k+1) = i_{sd}^{s}(k) + \left(\frac{T_s}{a}\right) \times \begin{Bmatrix} v_{sd}^{s}(k) - bv_{pd}^{s}(k) - cv_{pq}^{s}(k) + di_{pd}^{s}(k) \\ -ei_{pq}^{s}(k) - R_s i_{sd}^{s}(k) + fi_{sq}^{s}(k) \end{Bmatrix} \tag{17}$$

$$i_{sq}^{s*}(k+1) = i_{sq}^{s}(k) + \left(\frac{T_s}{a}\right) \times \begin{Bmatrix} v_{sq}^{s}(k) - cv_{pd}^{s}(k) + bv_{pq}^{s}(k) - ei_{pd}^{s}(k) \\ -di_{pq}^{s}(k) - fi_{sd}^{s}(k) - R_s i_{sq}^{s}(k) \end{Bmatrix}. \tag{18}$$

Herein, (17) and (18) are used as the predictors of the secondary currents. Furthermore, $i_{sd}^{s*}(k+1)$ and $i_{sq}^{s*}(k+1)$ are utilized in the second stage for more correct final predictions of $i_{sd}^{s}(k+1)$ and $i_{sq}^{s}(k+1)$ as

$$i_{sd}^{s}(k+1) = i_{sd}^{s}(k) + \left(\frac{T_s}{a}\right) \times \begin{bmatrix} v_{sd}^{s}(k) - bv_{pd}^{s}(k) - cv_{pq}^{s}(k) + di_{pd}^{s}(k) - ei_{pq}^{s}(k) \\ -R_s\left\{\frac{i_{sd}^{s}(k)+i_{sd}^{s*}(k+1)}{2}\right\} + f\left\{\frac{i_{sq}^{s}(k)+i_{sq}^{s*}(k+1)}{2}\right\} \end{bmatrix} \tag{19}$$

$$i_{sq}^{s}(k+1) = i_{sq}^{s}(k) + \left(\frac{T_s}{a}\right) \times \begin{bmatrix} v_{sq}^{s}(k) - cv_{pd}^{s}(k) + bv_{pq}^{s}(k) - ei_{pd}^{s}(k) - di_{pq}^{s}(k) \\ -f\left\{\frac{i_{sd}^{s}(k)+i_{sd}^{s*}(k+1)}{2}\right\} - R_s\left\{\frac{i_{sq}^{s}(k)+i_{sq}^{s*}(k+1)}{2}\right\} \end{bmatrix}. \tag{20}$$

Equations (19) and(20) can further be simplified as

$$i_{sd}^{s}(k+1) = i_{sd}^{s*}(k+1) + \left(\frac{T_s}{2a}\right) \times \begin{bmatrix} -R_s\left\{i_{sd}^{s*}(k+1) - i_{sd}^{s}(k)\right\} \\ +f\left\{i_{sq}^{s*}(k+1) - i_{sq}^{s}(k)\right\} \end{bmatrix} \tag{21}$$

$$i_{sq}^{s}(k+1) = i_{sq}^{s*}(k+1) + \left(\frac{T_s}{2a}\right) \times \begin{bmatrix} -R_s\left\{i_{sq}^{s*}(k+1) - i_{sq}^{s}(k)\right\} \\ -f\left\{i_{sd}^{s*}(k+1) - i_{sd}^{s}(k)\right\} \end{bmatrix}. \tag{22}$$

The second step of predictions, i.e., the calculation of $i_{sd}^{s}(k+2)$ and $i_{sq}^{s}(k+2)$ is presented in Section II-C.3.

2) Minimization of Objective Function: As different voltage vectors produce dissimilar current variations, it is necessary to evaluate the effect of each voltage vector individually and select the best one minimizing the current error. The evaluation is done in terms of an objective function expressed as

$$g_x = \left|i_{sd}^{s\_\mathrm{ref}} - i_{sd}^{s}(k+2)\right|^2 + \left|i_{sq}^{s\_\mathrm{ref}} - i_{sq}^{s}(k+2)\right|^2\Big|_{x=1:6}. \tag{23}$$

The calculation of the objective function is done for six active vectors. The minimum one is stored as g_{opt}. In the rest portion of the control interval, one of the two zero-voltage vectors is applied.

3) Duty-Cycle Determination: The optimal active voltage vector is applied for a fraction of the control period. In general, zero vectors produce moderate variations of current slopes; therefore, a zero vector can be used for the rest of the time interval. Consequently, two pairs of slopes must be calculated in each of the six steps. The current slopes caused by the optimal active vector v_{opt} and zero vector v_o are (s_{1d}, s_{1q}) and (s_{0d}, s_{0q}), respectively, where

$$s_{0d} = \left.\frac{di_{sd}^{s}}{dt}\right|_{v_{sd}^{s}=v_{0d}} = \left(\frac{1}{a}\right)\begin{Bmatrix} -bv_{pd}^{s} - cv_{pq}^{s} + di_{pd}^{s} \\ -ei_{pq}^{s} - R_s i_{sd}^{s} + fi_{sq}^{s} \end{Bmatrix} \tag{24}$$

$$s_{1d} = \left.\frac{di_{sd}^{s}}{dt}\right|_{v_{sd}^{s}=v_{\mathrm{opt\_}d}} = s_{0d} + \left(\frac{1}{a}\right) v_{\mathrm{opt\_}d} \tag{25}$$

$$s_{0q} = \left.\frac{di_{sq}^{s}}{dt}\right|_{v_{sq}^{s}=v_{0q}} = \left(\frac{1}{a}\right)\begin{Bmatrix} -cv_{pd}^{s} + bv_{pq}^{s} - ei_{pd}^{s} \\ -di_{pq}^{s} - fi_{sd}^{s} - R_s i_{sq}^{s} \end{Bmatrix} \tag{26}$$

$$s_{1q} = \left.\frac{di_{sq}^{s}}{dt}\right|_{v_{sq}^{s}=v_{\mathrm{opt\_}q}} = s_{0q} + \left(\frac{1}{a}\right) v_{\mathrm{opt\_}q}. \tag{27}$$

Finally, the predicted current components at instant $k+2$ are determined as

$$i_{sd}^{s}(k+2) = i_{sd}^{s}(k+1) + s_{1d}t_{\mathrm{opt}} + s_{0d}(T_s - t_{\mathrm{opt}}) \tag{28}$$

$$i_{sq}^{s}(k+2) = i_{sq}^{s}(k+1) + s_{1q}t_{\mathrm{opt}} + s_{0q}(T_s - t_{\mathrm{opt}}). \tag{29}$$

The optimal duration (t_{opt}) of the best active vector during one control period satisfies the following condition:

$$\partial g_{\mathrm{opt}}/\partial t_{\mathrm{opt}} = 0. \tag{30}$$

Substituting (28) and (29) into (23), and subsequently using (30), t_{opt} can be determined as

$$t_{\mathrm{opt}} = \frac{T_s\begin{pmatrix} s_{od}^2 - s_{0d}s_{1d} \\ -s_{0q}s_{1q} + s_{oq}^2 \end{pmatrix} + \begin{bmatrix} (s_{1d} - s_{0d})\{i_{sd}^{s\_\mathrm{ref}} - i_{sd}^{s}(k+1)\} \\ +(s_{1q} - s_{0q})\{i_{sq}^{s\_\mathrm{ref}} - i_{sq}^{s}(k+1)\} \end{bmatrix}}{(s_{0d} - s_{1d})^2 + (s_{0q} - s_{1q})^2} \tag{31}$$

where

$$t_{\mathrm{opt}} = \begin{cases} 0, & \text{if } t_{\mathrm{opt}} < 0 \\ T_s, & \text{if } t_{\mathrm{opt}} > T_s. \end{cases} \tag{32}$$

4) Selection of Switching States for 2L-VSI: The voltage vectors of 2L-VSI corresponding to their switching states and the switching patterns of MPCC involving duty-cycle control are shown in Fig. 2(a) and (b), respectively. The voltage vector magnitude corresponding to its switching state is given in [17, Table 4.2]. As seen in Fig. 2(b), the optimal voltage vector among six active vectors $(\boldsymbol{v}_{1:6})$ is applied for the optimal time duration(t_{opt}). While optimizing duty cycle, the magnitude of the applied voltage vector changes only and its direction remains

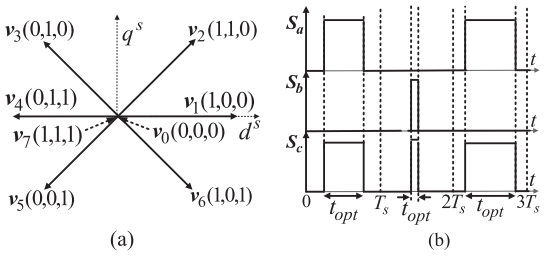

Fig. 2. Inverter switching. (a) Voltage vectors of 2L-VSI. (b) Switching in MPCC with duty-cycle calculation.

unchanged. The zero-voltage vector $(\boldsymbol{v}_{0/7})$, which requires the lowest number of switching transitions, is applied in the residual time interval $(T_s - t_{\rm opt})$. The algorithm of the above discussed current control method is summarized as follows:

1) measurement of $\boldsymbol{v_p^s}$, $\boldsymbol{i_p^s}$, and ω_{rm};
2) estimation of $\boldsymbol{\lambda_p^s}$, $\boldsymbol{i_s^s}$,θ_p,θ_s, and θ_r;
3) calculation of $i_{sd}^{s\_\rm ref}$ and $i_{sq}^{s\_\rm ref}$;
4) first-stage prediction of $\boldsymbol{i_s^s}$ (21), (22)

$$\boldsymbol{i_s^s}(k+1) = f_1\{\boldsymbol{v_p^s}, \boldsymbol{i_p^s}(k), \boldsymbol{i_s^s}(k), \boldsymbol{v_{opt}}\};$$

5) for $x = 1{:}6$, calculation of duty cycle (31)

$$t_{\rm opt\_}x = f_2\{\boldsymbol{i_s^s}(k+1), \boldsymbol{i_s^{s\_ref}}(k+1), s_{1\_}x, s_0\};$$

6) second-stage prediction of $\boldsymbol{i_s^s}$ (28), (29)

$$\boldsymbol{i_s^s}(k+2) = f_3\{\boldsymbol{i_s^s}(k+1), s_{1\_}x, s_0, t_{\rm opt\_}x\};$$

7) calculation of objective function (23)

$$g_x = f_4\{\boldsymbol{i_s^{s\_ref}}, \boldsymbol{i_s^s}(k+2)\};$$

8) if $g_x >= g$ then go to step 10;
9) else $g_{\rm opt} = g_x$, $\boldsymbol{v_{opt}} = \boldsymbol{v_x}$, $s_1 = s_{1\_}x$; $t_{\rm opt} = t_{\rm opt\_}x$;
10) increment of x by 1;
11) if $(x < 6)$ then go to step 5;
12) application of switching states corresponding to $\boldsymbol{v_{opt}}, \boldsymbol{v}_{\rm o}$ for $t_{\rm opt}$, $(T_s - t_{\rm opt})$ interval, respectively.

III. Simulation and Experimental Results

The performance of the proposed control scheme has been investigated extensively for 30% of speed variations around synchronous speed through simulations in MATLAB/Simulink. The method is also executed for real-time experimentations using dSPACE-1103. The machine specifications are presented in Appendix A (see Table IV).

A. Simulation Results

A few simulation results are shown in this section to illustrate the drive performance for the constant-torque variable-speed maneuver for the proposed MPCC strategy in motoring and generating modes.

Fig. 3 represents the drive performance in the motoring mode of operation at 9 N·m load torque. As shown in Fig. 3(a), the rotor speed tracks the reference speed smoothly throughout the speed control range. Fig. 3(b) depicts the absolute speed error in the whole speed ranges whose amplitude lies below 10 r/min

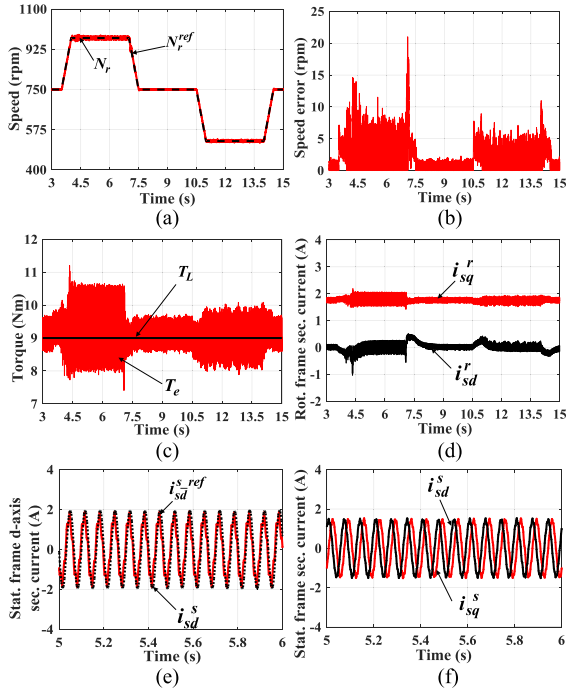

Fig. 3. Simulation results-1: Variable-speed (750-974-750-525 r/min) and constant-torque (9 N·m/ 0.5 p.u. motoring mode) operation under MPCC scheme. (a) Speed tracking performance. (b) Absolute speed error. (c) Torque patterns. (d) Rotating frame secondary currents. (e) Stationary frame d-axis secondary current reference tracking. (f) Stationary frame secondary currents.

in steady state and seldom surges up to 20 r/min during speed transients. Fig. 3(c) shows the torque profile. The electromagnetic torque behaves smoothly during the transient period also with the acceptable amount of ripples all over. The decoupled i_{sd}^r and i_{sq}^r in Fig. 3(d) signify the effectiveness of PFOC condition. The magnitude of i_{sq}^r is essentially constant for all operating speed under constant load torque condition. Moreover, i_{sd}^r remains zero throughout the MTPIA strategy of the drive. In Fig. 3(e), it is seen that i_{sd}^s follows its reference $i_{sd}^{s\_\rm ref}$ precisely. In Fig. 3(f), i_{sd}^s and i_{sq}^s are shown at supersynchronous speed. For the same amount of speed variation from supersynchronous to subsynchronous speed, the current frequencies remain the same but phase sequence reverses.

The variable-speed performance in the generating mode of the drive is represented in Fig. 4. As shown in Fig. 4(a), the speed of the machine tracks the reference speed precisely during the course of operation. The amplitude of absolute speed error is less than 5 r/min in the synchronous and supersynchronous speed regions but fluctuates between 10 and 20 r/min in subsynchronous speed ranges [see Fig. 4(b)]. Fig. 4(c) shows the primary active and reactive power profiles at 9 N·m shaft torque. The PFOC and MTPIA conditions are fulfilled in this case as well, as seen from i_{sd}^r and i_{sq}^r waveforms in Fig. 4(d). Fig. 4(e) and (f) show that i_{sd}^s follows $i_{sd}^{s\_\rm ref}$ satisfactorily and leads i_{sq}^s by 90° in the supersynchronous speed region. The primary winding is connected to a grid at 415 V [see Fig. 4(g)]. However, the secondary voltage is decided by the constant dc-link voltage and the switching-state vector [see Fig. 4(h)].

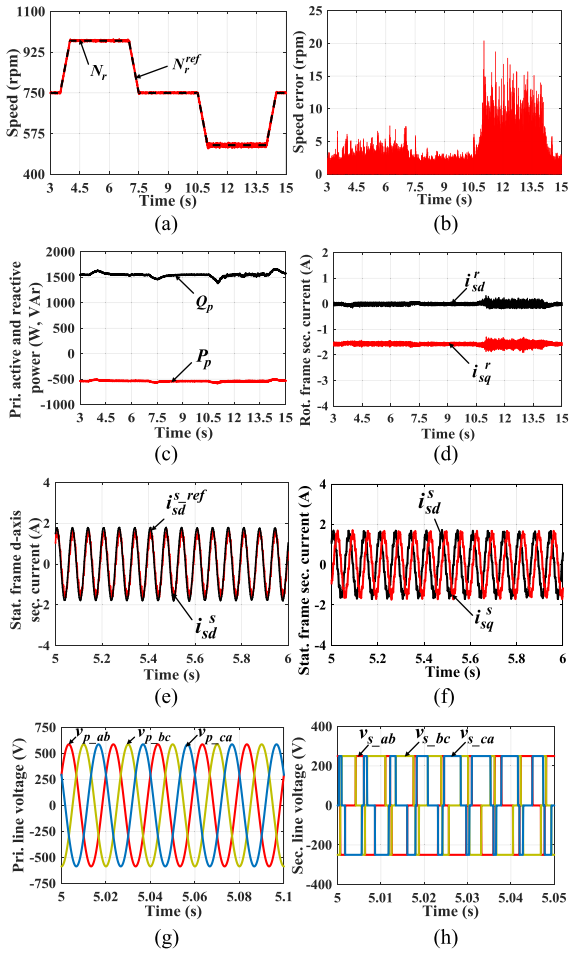

Fig. 4. Simulation results-2: Variable-speed (750-974-750-525 r/min) and constant-torque (−9 N·m /−0.5 p.u. generating mode) operation under MPCC scheme. (a) Speed tracking performance. (b) Absolute speed error. (c) Primary power. (d) Rotating frame secondary currents. (e) Stationary frame *d*-axis secondary current reference tracking. (f) Stationary frame secondary currents. (g) Primary line voltages. (h) Secondary line voltages.

B. Experimental Validations

The schematic block diagram and the laboratory prototype experimental setup are shown in Fig. 5. The system comprises a BDFRM with its rotor directly coupled to a separately excited dc machine. The rotor speed, primary phase currents, and line voltages are sensed and fed to the analog-to-digital converter ports of the dSPACE-1103 controller board for the execution of the control algorithms. The primary winding of the machine is directly connected to mains at 50 Hz, and the secondary winding is driven by a three-phase inverter for the bidirectional power flow depending upon the operating speed mode. The switches of the inverter operate at 20 kHz sampling frequency. The inverter utilizes 250 V dc-link voltages for 30% of speed regulation around the synchronous speed. The experiment is conducted at 4.5 N·m load torque for the motoring (see Fig. 6) and generating (see Fig. 7) modes of operation for variable speed conditions. This is to mention here that the experimentation on higher load is restricted by excessive heating perhaps due to some constructional flaw in the machine.

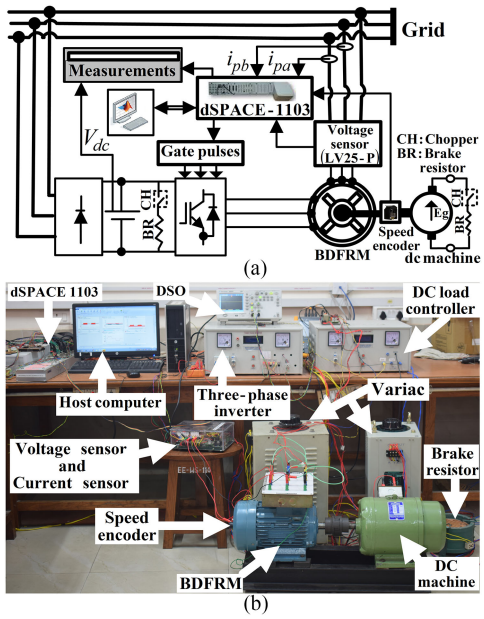

Fig. 5. Experimental setup of BDFRM drive. (a) Schematic layout. (b) Laboratory prototype.

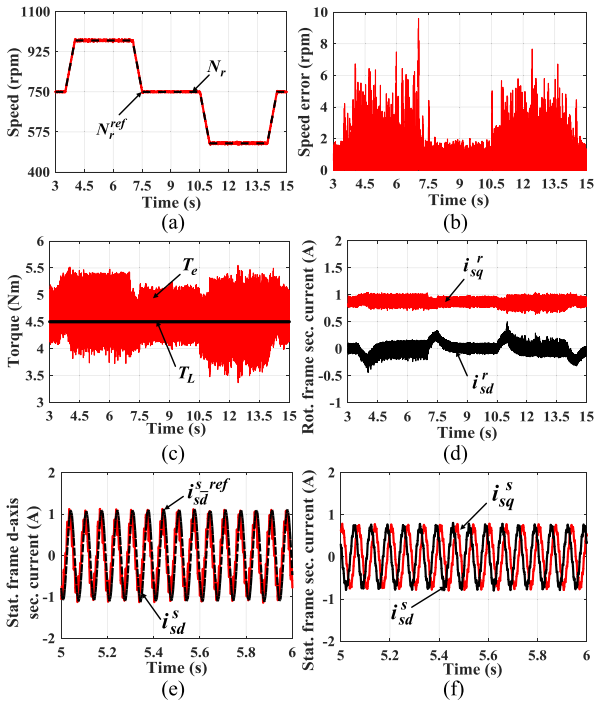

Fig. 6. Experimental results-1: Variable-speed (750-974-750-525 r/min) and constant-torque (4.5 N·m/0.25 p.u. motoring mode) operation under MPCC scheme. (a) Speed tracking performance. (b) Absolute speed error. (c) Torque patterns. (d) Rotating frame secondary currents. (e) Stationary frame *d*-axis secondary current reference tracking. (f) Stationary frame secondary currents.

Figs. 6(a) and 7(a) show that the machine speed tracks the trapezoidal pattern of reference speed very promptly and smoothly with acceptable speed error, as seen in Figs. 6(b) and 7(b). Fig. 6(c) reveals the electromagnetic torque behavior of the motor drive at one-fourth of the rated load torque. However,

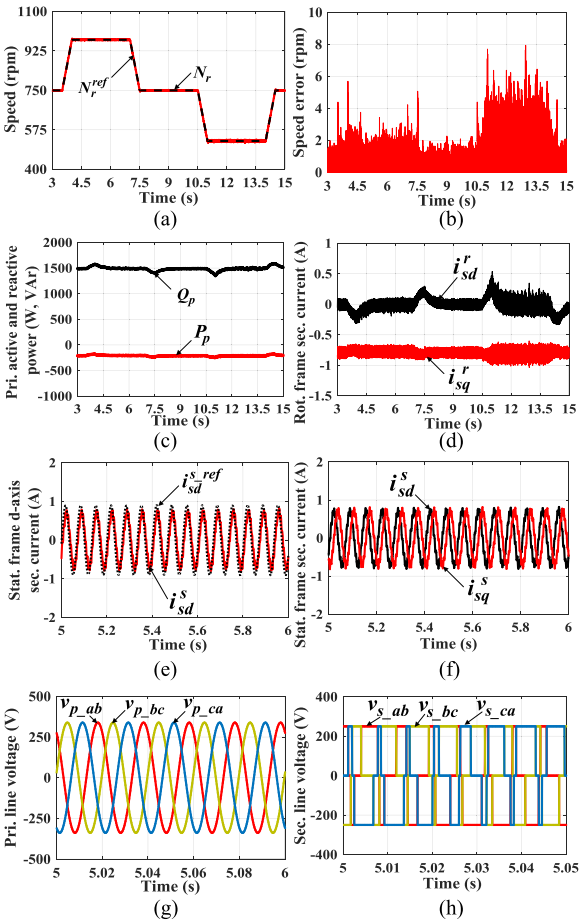

Fig. 7. Experimental results-2: Variable-speed (750-974-750-525 r/min) and constant-torque (−4.5 N·m/−0.25 p.u. generating mode) operation under MPCC scheme. (a) Speed tracking performance. (b) Absolute speed error. (c) Primary power. (d) Rotating frame secondary currents. (e) Stationary frame d-axis secondary current reference tracking. (f) Stationary frame secondary currents. (g) Primary line voltages. (h) Secondary line voltages.

Fig. 7(c) portrays the active and reactive power flow in the primary winding of the machine at 4.5 N·m shaft torque. The PFOC and MTPIA strategies are assured all over, as demonstrated in Figs. 6(d) and 7(d). Figs. 6(e) and 7(e) depict the tracking from i_{sd}^{s} to $i_{sd}^{s\_\mathrm{ref}}$. Moreover, Figs. 6(f) and 7(f) characterize the phase sequence relationship of i_{sd}^{s} and i_{sq}^{s}. The voltages of the primary and secondary windings are represented in Fig. 7(g) and (h), respectively.

IV. Performance Assessment

The aspects of the drive performance under the proposed MPCC scheme and standard FOC strategy as a benchmark are compared with the same test-rig off-line in MATLAB/Simulink at different load torques. The steady-state behavior of the drive systems in terms of speed ripple, torque ripple, and total harmonic distortion (THD) in secondary current at different operating points is organized in Table I. The transient responses of the controllers for step speed change from 750 to 974 r/min are presented in Table II. In addition, the sensitivity analysis against parameter variations in the case of the proposed MPCC is also done in this section.

TABLE I
Steady-State Comparative Performance [RMSSE: r/min, RMSTE: N·m]

Operating Speed		525 rpm		750 rpm		974 rpm	
Load	Index	MPCC	FOC	MPCC	FOC	MPCC	FOC
13.5 Nm	RMSSE	2.68	1.26	0.90	0.37	3.02	22.60
	RMSTE	0.38	0.23	0.33	0.12	0.38	0.95
	%THD$_i$	5.29	1.95	-	-	5.79	22.25
9 Nm	RMSSE	2.15	1.68	0.90	0.22	2.53	1.46
	RMSTE	0.36	0.22	0.34	0.12	0.37	0.29
	%THD$_i$	5.73	4.21	-	-	6.33	4.54
4.5 Nm	RMSSE	1.78	1.42	0.82	0.15	1.46	1.26
	RMSTE	0.32	0.20	0.33	0.12	0.37	0.20
	%THD$_i$	11.48	7.60	-	-	11.51	6.67
-4.5 Nm	RMSSE	1.94	1.15	1.12	0.22	1.85	1.65
	RMSTE	0.29	0.22	0.35	0.12	0.38	0.18
	%THD$_i$	11.78	7.60	-	-	12.64	8.20
-9 Nm	RMSSE	3.15	2.57	2.10	0.22	2.43	2.04
	RMSTE	0.31	0.24	0.34	0.10	0.40	0.35
	%THD$_i$	6.90	6.06	-	-	6.25	4.37
-13.5 Nm	RMSSE	3.73	2.94	2.32	0.30	6.33	4.38
	RMSTE	0.34	0.27	0.35	0.12	0.41	0.30
	%THD$_i$	5.77	31.1	-	-	5.29	2.66

TABLE II
Transient-State Comparative Performance

Index	Step change in speed (750 rpm to 974 rpm)	
	MPCC	FOC
Rise Time (ms)	23.6	38.5
Settling Time (ms)	125	122
Peak Overshoot (%)	6.43	10.00

A. Comparative Study of Steady State and Dynamic Behavior

The performance indices to judge the excellence of the proposed method in terms of torque and speed ripples are obtained by root-mean-square speed error (RMSSE), root-mean-square torque error (RMSTE) (see Appendix B), and percentage THD in the secondary current waveform.

Table I lists that the FOC-based controller prevails over the MPCC scheme concerning the steady-state performance due to the presence of inner current PI controllers and PWM in the former but at the cost of higher switching losses. However, the performance of MPCC, including the duty-cycle control concept, is also remarkable. The synchronous speed performance of the drive is very smooth with lowest ripple in speed and torque. The speed error increases with the speed variation around the synchronous speed. It is observed that the torque ripple decreases and speed ripple increases with the increase in torque at any speed. However, the system becomes unstable at some operating points at high load torque. Due to the involvement of less number of PI controllers, the region of stable operation of the MPCC-based drive is wider than that of the FOC-based drive. In the case of MPCC control, the percentage THD in secondary current is also within a satisfactory range.

The excellence of the drive under the proposed scheme in respect of transient response is given in Table II. It can be observed that the dynamic response of the proposed MPCC scheme is improved significantly than FOC-based approach in terms of rise time and percentage peak overshoot. However, the settling time required to bring the rotor speed to its reference value in the case of MPCC is marginally sluggish than that of FOC.

TABLE III
RMSSE (r/min) IN STEADY STATE FOR PARAMETER VARIATIONS

Parameter↓	Speed (rpm)↓	T_L (Nm)					
		13.5	9	4.5	-4.5	-9	-13.5
$2R_p$	525	3.21	2.42	1.85	1.96	4.01	13.54
remaining	750	1.35	1.27	1.03	1.29	2.16	4.35
nominal	974	3.78	2.58	2.01	2.14	2.63	7.60
$2R_s$	525	2.86	2.33	1.76	2.25	3.81	10.18
remaining	750	1.05	0.97	0.90	1.15	2.11	2.55
nominal	974	3.44	2.55	1.94	1.96	2.63	6.72
1.3 L_s	525	2.67	2.34	1.83	2.00	3.66	9.33
remaining	750	0.90	1.01	0.97	1.22	1.95	2.47
nominal	974	2.84	2.56	1.62	2.04	28.15	13.25

B. Influence of Parameter Mismatch and Variations

The MPCC uses the machine model; therefore, the exact information of system parameters is crucial for good control quality. However, it is not possible to get their precise values due to the measurement imperfections, temperature variations, instance disturbances, saturation, and time delay. With these limitations, the drive system performance may deteriorate to violate the PFOC and MTPIA strategies or worsen up to instability. BDFRM operates at almost constant-rated primary flux due to the direct connection to the grid. This leads to a minimal variation in primary self- and mutual inductances under all the operating conditions. Therefore, the effect of variations of secondary inductance is analyzed here only. In addition, the resistances of an electric machine increase noticeably during continuous operation under loaded conditions due to temperature variations. Therefore, the impact of primary and secondary winding resistance variations on the drive's performance is studied at subsynchronous (525 r/min), synchronous (750 r/min), and supersynchronous (974 r/min) speeds for different load torques in MATLAB/Simulink.

In Table III, the performance analysis is done for 100% changes in primary and secondary resistances and 30% variations in secondary inductance individually in the controller keeping the other parameters at their nominal values. It is observed that the controller responds satisfactorily even for these abnormal changes reflecting marginal upsurge of ripples in torque and speed profiles under the investigated range.

V. CONCLUSION

In this article, the MPCC strategy is proposed for the field-oriented speed control of the BDFRM drive. The MPCC controller comprises the concept of duty-cycle control to increase the degree of freedom with regard to the switching states of 2L-VSI. In this respect, a zero-voltage vector is allocated in the control algorithm for a fraction of one control period along with an optimal active voltage vector because it produces the smallest change in control variables. The optimal duration for the application of the active- and zero-voltage vectors is based on the minimization of corresponding current slopes.

The scheme is experimentally validated for the speed control of BDFRM drive in motoring and generating regimes. The relative merits of the proposed scheme over the conventional FOC scheme are emphasized. The scheme has significant advantages of a good dynamic state at lower switching losses than FOC. The design aspects of the proposed technique are enlisted as follows.

1) The use of secondary current as a control variable makes the MPCC scheme analogous to FOC.
2) Execution of the algorithm in the stationary reference frame requires a lesser number of axes transformations.
3) The absence of inner current PI controllers avoids the hectic tuning of PI controller gains, increases the bandwidth of operating regions, and improves the dynamic performance of the drive system.
4) The use of a discrete system model for the direct generation of switching states of the inverter excludes the involvement of any PWM; thus, the implementation complexity is reduced.
5) Secondary current error based online optimization algorithm attributes good speed tracking performance.
6) The inclusion of the duty-cycle concept in the control algorithm improves the steady-state performance of the drive system by reducing current ripples.

Similar to the conventional MPCC approaches, the involvement of the enumeration-based objective function evaluation combined with the duty-cycle calculation further intensifies the computation process of the present approach. As a result, the fast-acting processor is also mandatory for its real-time implementation. In addition, the principle of deadbeat control can be embraced to tackle the control complexity and the computational burden. Moreover, the controller performance against machine parameter variations can be resolved with suitable estimation techniques.

APPENDIX A

TABLE IV
MACHINE SPECIFICATIONS FOR THE PROPOSED WORK

BDFRM rating		DC machine rating	
Rated power	1.6 kW	Rated power	1.5 kW
Current	3/ 2.3 A	Rated current	8 A
Line voltage	415/415 V	Rated voltage	220 V
Primary supply frequency	50 Hz	Rated speed	1500 rpm
No. of rotor, primary and secondary poles	4, 6, 2	Type	Separately -excited
Primary and secondary winding resistances	10.2 Ω, 12.8 Ω	Duty	CMR (S1)
Primary and secondary winding self-inductances	0.38 H, 0.54 H		
Primary and secondary winding mutual inductance	0.32 H		
Rotor inertia	0.035 kg m^2		
Friction coefficient	0.0014		

APPENDIX B

RMSTE and RMSSE can be expressed as

$$\mathrm{RMSTE} = \frac{1}{N}\sqrt{\sum_{k=1}^{N}\left(T_L - T_e\left(k\right)\right)^2} \tag{B1}$$

$$\mathrm{RMSSE} = \frac{1}{N}\sqrt{\sum_{k=1}^{N}\left(N_r^{\mathrm{ref}} - N_r\left(k\right)\right)^2} \tag{B2}$$

where N is the number of discrete samples over a period of 10 s.

REFERENCES

[1] P. Han, M. Cheng, S. Ademi, and M. G. Jovanovic, "Brushless doubly-fed machines: Opportunities and challenges," *Chin. J. Elect. Eng.*, vol. 4, no. 2, pp. 1–17, Jun. 2018.

[2] S. Abdi, E. Abdi, and R. McMahon, "A light-weight rotor design for brushless doubly fed machines," in *Proc. 13th Int. Conf. Elect. Mach.*, Alexandroupoli, Greece, Sep. 3–6, 2018, pp. 493–498.

[3] R. Cárdenas, R. Pena, S. Alepuz, and G. Asher, "Overview of control systems for the operation of DFIGs in wind energy applications," *IEEE Trans. Ind. Electron.*, vol. 60, no. 7, pp. 2776–2798, Jul. 2013.

[4] R. E. Betz and M. Jovanovic, "Introduction to brushless doubly fed reluctance machines—The basic equations," Aalborg Univ., Aalborg, Denmark, Tech. Rep. EEO023, Mar. 2012.

[5] F. Zhang, S. Yu, H. Wang, Y. Wang, and D. Wang, "Overview of research and development status of brushless doubly-fed machine system," *Chin. J. Elect. Eng.*, vol. 2, no. 2, pp. 1–13, Dec. 2016.

[6] F. Wang, F. Zhang, and L. Xu, "Parameter and performance comparison of doubly fed brushless machine with cage and reluctance rotors," *IEEE Trans. Ind. Appl.*, vol. 38, no. 5, pp. 1237–1243, Sep./Oct. 2000.

[7] M. G. Jovanovic, R. E. Betz, and J. Yu, "The use of doubly fed reluctance machines for large pumps and wind turbines," *IEEE Trans. Ind. Appl.*, vol. 38, no. 6, pp. 1508–1516, Nov./Dec. 2002.

[8] S. Ademi and M. G. Jovanovic, "Vector control methods for brushless doubly-fed reluctance machines," *IEEE Trans. Ind. Electron.*, vol. 62, no. 1, pp. 96–104, Jan. 2015.

[9] M. Jovanovic, "Sensored and sensorless speed control methods for brushless doubly fed reluctance motor," *IET Electr. Power Appl.*, vol. 3, no. 6, pp. 503–513, Nov. 2009.

[10] H. Chaal and M. Jovanovic, "Direct power control of brushless doubly-fed reluctance machines," in *Proc. 5th IET Int. Conf. Power Electron., Mach. Drives*, Brighton, U.K., Apr. 19–21, 2010.

[11] L. Xu, L. Zhen, and E.-H. Kim, "Field-orientation control of a doubly excited brushless reluctance machine," *IEEE Trans. Ind. Appl.*, vol. 34, no. 1, pp. 148–155, Jan./Feb. 1998.

[12] K. Kiran and S. Das, "Implementation of reactive power-based MRAS for sensorless speed control of brushless doubly fed reluctance motor drive," *IET Power Electron.*, vol. 11, no. 1, pp. 192–201, Feb. 2018.

[13] M. Kumar, S. Das, and K. Kiran, "Sensorless speed estimation of brushless doubly-fed reluctance generator using active power based MRAS," *IEEE Trans. Power Electron.*, vol. 34, no. 8, pp. 7878–7886, Aug. 2019.

[14] Y. Zhang and J. Zhu, "Direct torque control of permanent magnet synchronous motor with reduced torque ripple and commutation frequency," *IEEE Trans. Power Electron.*, vol. 26, no. 1, pp. 235–248, Jan. 2011.

[15] J. Rodriguez *et al.*, "Predictive current control of a voltage source inverter," *IEEE Trans. Ind. Electron.*, vol. 54, no. 1, pp. 495–503, Feb. 2007.

[16] H. A. Young, M. A. Perez, and J. Rodriguez, "Analysis of finite-control-set model predictive current control with model parameter mismatch in a three-phase inverter," *IEEE Trans. Ind. Electron.*, vol. 63, no. 5, pp. 3100–3107, May 2016.

[17] J. Rodriguez and P. Cortes, *Predictive Control of Power Converters and Electrical Drives*. Valparasio, Chile: Wiley, 2012.

[18] M. Moazen, R. Kazemzadeh, and M.-R. Azizian, "Model-based predictive direct power control of brushless doubly fed reluctance generator for wind power applications," *Alexandria Eng. J.*, vol. 55, no. 3, pp. 2497–2507, Sep. 2016.

[19] E. Fuentes, J. Rodrigues, C. Silva, S. Diaz, and D. E. Quevedo, "Speed control of a permanent magnet synchronous motor using predictive current control," in *Proc. IEEE Int. Power Electron. Motion Control Conf.*, Wuhan, China, May 17–20, 2009, pp. 390–395.

[20] H.-T. Moon, H.-S. Kim, and M.-J. Youn, "A discrete-time predictive current control for PMSM," *IEEE Trans. Power Electron.*, vol. 18, no. 1, pp. 464–472, Jan. 2003.

[21] F. Wang, X. Mei, P. Tao, R. Kennel, and J. Rodriguez, "Predictive field-oriented control for electric drives," *Chin. J. Elect. Eng.*, vol. 3, no. 1, pp. 73–78, Jun. 2017.

[22] F. Wang, S. Li, X. Mei, W. Xie, J. Rodríguez, and R. Kennel, "Model-based predictive direct control strategies for electrical drives: An experimental evaluation of PTC and PCC methods," *IEEE Trans. Ind. Inform.*, vol. 11, no. 3, pp. 671–681, Jun. 2015.

[23] M. A. Mossa and S. Bolognani, "Effective model predictive current control for a sensorless IM drive," in *Proc. IEEE Int. Symp. Sensorless Control Elect. Drives*, Catania, Italy, Sep. 2017, pp. 37–42.

[24] A. Darba, F. de Belie, P. D'haese, and J. A. Melkebeek, "Improved dynamic behavior in BLDC drives using model predictive speed and current control," *IEEE Trans. Ind. Electron.*, vol. 63, no. 2, pp. 728–740, Feb. 2016.

[25] Y. Zhang, D. Xu, J. Liu, S. Gao, and W. Xu, "Performance improvement of model predictive current control of permanent magnet synchronous motor drives," *IEEE Trans. Ind. Appl.*, vol. 53, no. 4, pp. 3683–3695, Jul./Aug. 2017.

[26] S.-C. Carpiuc and C. Lazar, "Fast real-time constrained predictive current control in permanent magnet synchronous machine-based automotive traction drives," *IEEE Trans. Transp. Electrific.*, vol. 1, no. 4, pp. 326–335, Dec. 2015.

[27] Y. Zhang and H. Yang, "Model predictive torque control of induction motor drives with optimal duty cycle control," *IEEE Trans. Power Electron.*, vol. 29, no. 12, pp. 6593–6603, Dec. 12, 2014.

[28] K. Kiran, S. Das, and D. Singh, "Model predictive field oriented speed control of brushless doubly-fed reluctance motor drive," in *Proc. Int. Conf. Power, Instrum., Control Comput.*, Thrissur, India, Jan. 18–20, 2018.

[29] Y. Zhang, J. Zhu, and W. Xu, "Analysis of one step delay in direct torque control of permanent magnet synchronous motor and its remedies," in *Proc. Int. Conf. Elect. Mach. Syst.*, Incheon, South Korea, Oct. 10–13, 2010, pp. 792–797.

[30] S. Chapra and R. Canale, *Numerical Methods for Engineers*, 6th ed. New York, NY, USA: McGraw-Hill, 2010.

Karuna Kiran (Student Member, IEEE) received the B.Tech. degree in electrical and electronics engineering from Aryabhatta Knowledge University, Patna, India, in 2012. She is currently working toward the Ph.D. degree in electrical engineering with the Indian Institute of Technology (Indian School of Mines), Dhanbad, India.

Her research interests include machine drives and power electronics.

Sukanta Das (Senior Member, IEEE) received the B.E. degree in electrical engineering from Jalpaiguri Government Engineering College, Jalpaiguri, India, in 2002, and the M.E. and Ph.D. degrees in electrical engineering from Bengal Engineering and Science University (now known as the Indian Institute of Engineering Science and Technology), Howrah, India, in 2004 and 2013, respectively.

He is currently an Assistant Professor with the Department of Electrical Engineering, Indian Institute of Technology (Indian School of Mines), Dhanbad, India. He has authored/coauthored about 50 publications in journals/conferences. His research interests include electrical machine drives and power quality.